HAL
open science

Two-phase dynamics of volcanic eruptions: Particle size distribution and the conditions for choking

Viktoriya M. Yarushina, David Bercovici, Chloé Michaut

To cite this version:

Viktoriya M. Yarushina, David Bercovici, Chloé Michaut. Two-phase dynamics of volcanic eruptions: Particle size distribution and the conditions for choking. Journal of Geophysical Research : Solid Earth, 2015, 120, pp.1503-1522. 10.1002/2014JB011195 . insu-03580011

HAL Id: insu-03580011

https://insu.hal.science/insu-03580011

Submitted on 18 Feb 2022

HAL is a multi-disciplinary open access archive for the deposit and dissemination of scientific research documents, whether they are published or not. The documents may come from teaching and research institutions in France or abroad, or from public or private research centers.

L'archive ouverte pluridisciplinaire **HAL**, est destinée au dépôt et à la diffusion de documents scientifiques de niveau recherche, publiés ou non, émanant des établissements d'enseignement et de recherche français ou étrangers, des laboratoires publics ou privés.

Copyright

AGU PUBLICATIONS

JGR

Journal of Geophysical Research: Solid Earth

RESEARCH ARTICLE

10.1002/2014JB011195

Key Points:
- Effect of particle size distribution on volcanic eruptions is examined
- Phase separation leads to frequency separation for fast and slow waves
- Unimodal versus bimodal distributions can distinguish vertical and lateral eruptions

Correspondence to:
V. M. Yarushina,
viktoriya.yarushina@ife.no

Citation:
Yarushina, V. M., D. Bercovici, and C. Michaut (2015), Two-phase dynamics of volcanic eruptions: Particle size distribution and the conditions for choking, *J. Geophys. Res. Solid Earth*, *120*, 1503–1522, doi:10.1002/2014JB011195.

Received 15 APR 2014
Accepted 29 JAN 2015
Accepted article online 3 FEB 2015
Published online 18 MAR 2015

This is an open access article under the terms of the Creative Commons Attribution-NonCommercial-NoDerivs License, which permits use and distribution in any medium, provided the original work is properly cited, the use is non-commercial and no modifications or adaptations are made.

Two-phase dynamics of volcanic eruptions: Particle size distribution and the conditions for choking

Viktoriya M. Yarushina[1], David Bercovici[2], and Chloé Michaut[3]

[1]Department of Environmental Technology, Institute for Energy Technology, Kjeller, Norway, [2]Department of Geology and Geophysics, Yale University, New Haven, Connecticut, USA, [3]Laboratoire de Géophysique Spatiale et Planétaire, Université Paris Diderot, IPGP, Paris, France

Abstract Explosive volcanic eruptions are studied using a two-phase model of polydisperse suspensions of solid particles in gas. Eruption velocities depend on choking conditions in the volcanic conduit, which depend on acoustic wave propagation that is, in turn, influenced by the particle size distribution in the two-phase mixture. The acoustic wave spectrum is divided into three regions of superfast short waves moving at the pure gas sound speed, purely attenuated domain at intermediate wavelengths, and slower long waves for a dusty pseudogas. The addition of solid phases with differing particle sizes qualitatively preserves the features of two-phase acoustic wave dispersion, although it narrows the regions of short-fast and intermediate-blocked waves. Choking conditions, however, strongly depend on the number and size distribution of solid phases. Changes in particle sizes lead to variations in the choking conditions, which determine the eruption velocities and the resulting height of the erupting column. Smaller particles always exit the choking point faster than big particles, as expected. Even though particle-particle interaction is neglected, the particle distributions influence each other by momentum exchange through the gas. Therefore, the structure of the dispersion relation as well as the eruption or choking velocities and subsequent column height and particle deposition bear information on how eruption dynamics are controlled by size distribution and relative volume fractions of small and big particles. We suggest that unimodal distributions, with one dominant small particle size, favor development of vertical plinian eruptions, while bimodal distributions, with a comparable mean size, lead to pyroclastic lateral flows.

1. Introduction

Eruptions of silicic volcanoes are one of nature's most dramatic phenomena. Explosive eruptions typically follow fragmentation of vesicular magma in the volcanic conduit, leading to an ash-gas mixture, which rapidly decompresses and accelerates toward turbulent flow. Whether the mixture exiting the vent forms a plinian column or a pyroclastic flow depends on its two-phase dynamics, and in particular, on the eruption rate and gas volume fraction [*Wilson et al.*, 1980; *Woods*, 1995]. For example, the rate of phase separation and interphase drag controls the gas density, pressure, and volume fraction. Thus, the two-phase physics of mixtures in the volcanic conduit dictates the character of the explosive eruption.

Fluid dynamical models for volcanic eruptions often use the *pseudogas approximation*, wherein the ash-gas mixture acts as a single-phase medium in which the phases have identical velocities [*Jaupart and Tait*, 1990; *Woods*, 1995]. This approximation is important for predicting choking conditions, which determine the maximum flow velocities in a conduit. Choking occurs when expanding and accelerating flows approach the sound speed and then cannot, in principle, go any faster because they are impervious to any pressure changes inside or outside of the volcanic conduit [*John*, 1969; *Vergniolle and Jaupart*, 1986; *Wilson et al.*, 1980]. The effective sound speed in a pseudogas is much less than for a pure gas [see *Drew and Passman*, 1999, chap. 22] because mixture incompressibility is dominated by that of the gas, but its inertia is determined by the mixture density. The pseudogas model therefore predicts choking in the conduit at low velocities, between 100 and 200 m/s [*Bercovici and Michaut*, 2010]. Eruptions velocities, however, are estimated to be as high as 600 m/s [*Wilson*, 1976; *Wilson et al.*, 1980], which is similar to the pure gas sound speed (primarily of water vapor at 1000 K) and much larger than the pseudogas sound speed [*Kieffer*, 1977]. If the choking condition is determined by the slow pseudogas sound speed, then eruption speeds of 600 m/s would appear to be supersonic. This "slow choking" paradox is usually circumvented by appealing to nozzle effects in the conduit [*Mitchell*, 2005; *Wilson et al.*, 1980] wherein a de Laval jet engine-type converging-diverging

©2015. The Authors.

nozzle [*John*, 1969] permits supersonic velocities downstream of the choking point. However, slow choking at the pseudogas sound speed is a questionable assumption: the pseudogas model is a long-wavelength approximation [*Drew and Passman*, 1999], while acoustic shocks and choking are by definition short-wavelength effects. With phase separation that occurs for short wavelengths or high frequencies, the choking condition is significantly modified [*Bercovici and Michaut*, 2010; *Kozono and Koyaguchi*, 2009a, 2009b; *Vergniolle and Jaupart*, 1986] and is typically dictated by pure gas sounds speed of 600–700 m/s.

Fragmentation also plays an important role in the dynamics of conduit eruption, since it produces a wide distribution of magma particle sizes, from micrometer ashes to meter-sized blocks [*Kaminski and Jaupart*, 1998; *Walker*, 1980]. In particular, the quantity of fine ash ($<$300 μm) and very fine ash ($<$30 μm) in eruption products has become an increasingly active research area because of their respiratory health hazards and their deleterious impact on aircraft operations. Fine ash content has not been extensively studied in the past since such ash is difficult to sample and is easily eroded and transported away from their original locus of deposition. However, fairly recent studies reveal that the proportion of fine to very fine ash can be important, in particular for silicic eruptions, which can contain up to 30 to $>$50 wt % of very fine ash, in contrast to more mafic explosive eruptions that contain a smaller proportion (1–4 wt %) [*Rose and Durant*, 2009]. These new data also indicate that silicic eruptions may produce polymodal particle size distribution with a significant proportion of fine particles; such eruptions are also associated with prominent pyroclastic flows [*Evans et al*., 2009; *Rose and Durant*, 2009]. However, it is not clear how much of the fine ash is generated during the initial fragmentation sequence, or in the conduit and during explosive eruption at the volcanic vent [*Dufek et al*., 2012], or even by comminution within the pyroclastic density current itself [*Manga et al*., 2011]. Regardless of the cause for particle size distributions, the size influences the drag and turbulent interaction between solid and gas phases and thus their separation. For example, smaller and lighter particles are more easily carried by the gas phase than larger ones [*Chojnicki et al*., 2006] and likely influence shock development and choking. Hence, a significant fine ash component in the eruption product or a polymodal particle size distribution at the vent is likely to influence the eruption dynamics.

In this paper, we extend the theory for the dynamics of a turbulent mixture of gas with dispersed magma particles by *Bercovici and Michaut* [2010] and account for the presence of different population of particles with different sizes. The original model accounts for phase separation, which leads to gravitational settling, the interaction between compaction and gas compression, and simultaneous acoustic and porosity waves. Acoustic waves in particular are found to be very dispersive, wherein sound speeds and attenuation depend on wavelength and interphase drag. Indeed, the maximum sound speed occurs at shortest wavelengths and determines the choking condition (i.e., the maximum flow velocity that can be reached before a shock develops).

In this paper, we examine the impact of various size distributions on the two-phase dynamics of eruptions, and specifically on acoustic wave propagation and the implied choking conditions. In particular, while large particles will have more inertia, less drag, and be prone to phase separation, smaller particles might be more tightly coupled and phase-locked with the gas, giving it properties closer to that of a heavy pseudogas. Thus, the wavelength at which sound speed approaches that of a pure gas will be affected by the particle size distribution, which thus influences the choking condition. In the following sections we extend the two-phase theory for various particle size distributions, then examine their effect on linear acoustic waves, and finally analyze the nonlinear choking conditions at which a discontinuity or shock in gas density occurs. We show that the dynamics of an explosion at the vent might depend on whether the eruption products have a unimodal particle size distribution, which would favor a vertical eruption, or if it is polymodal, which would favor the appearance of lateral pyroclastic flows (possibly accompanied by an eruption column, depending on the details of the size distribution). Our model suggests that the presence of the second generation of particles is responsible for (1) different eruption styles, i.e., vertical plinian versus lateral (co) pyroclastic flows and (2) widening of the acoustic spectrum up to a few orders of magnitude. These phenomena cannot be captured without including the particle size distribution in the multiphase physics.

2. General 1-D Model of Two-Phase Flow With Particle Size Distribution

The presence of particles of different sizes in a volcanic flow during eruption are treated by assuming that the dispersed magma/ash phase can be divided into *m* fractions, each characterized by its own

©2015. The Authors.

particle size and velocity [*Nigmatulin*, 1991]. The mass conservation equation for the gas phase can still be written as

$$\frac{\partial \rho_g \varphi_g}{\partial t} + \frac{\partial \left(\rho_g \varphi_g v_g\right)}{\partial z} = 0 \tag{1}$$

while those for the solid phase particles ($i = 1, 2, \ldots, m$) is

$$\frac{\partial \varphi_i}{\partial t} + \frac{\partial (\varphi_i v_i)}{\partial z} = 0 \tag{2}$$

where ρ_g is density of carrying gas and φ_g and φ_i are volume fractions of gas and dispersed particles of type i, respectively, so that

$$\varphi_g + \sum_{i=1}^{m} \varphi_i = 1 \tag{3}$$

where v_g and v_i are the gas and particle velocities, respectively (and $v_g \neq v_i \neq v_j$ for $i \neq j$). We have assumed that magma particles are incompressible, and all have the same constant density ρ_m. We also assume that there is no mass exchange between solid and gaseous phases (i.e., no particle vaporization or condensation) and between different fractions of solid phase (i.e., no aggregation or fragmentation of particles due to collisions).

The conservation of momentum equations for the gas and particle phases are

$$\rho_g \varphi_g \frac{d_g v_g}{dt} = -\varphi_g \left(\frac{\partial p}{\partial z} + \rho_g g\right) + \sum_{i=1}^{m} I_{gi} \tag{4}$$

$$\rho_m \varphi_i \frac{d_i v_i}{dt} = -\varphi_i \left(\frac{\partial p}{\partial z} + \rho_i g\right) - I_{gi} + \sum_{j=1, j\neq i}^{m} I_{ji} \tag{5}$$

where g is gravity, p is gas pressure (which is assumed the same in each phase given the absence of surface tension and neglecting deformation of dispersed particles that might happen in densely packed mixtures) [see *Bercovici and Michaut*, 2010]. The material derivatives are defined as

$$\frac{d_g}{dt} = \frac{\partial}{\partial t} + v_g \frac{\partial}{\partial z}, \frac{d_i}{dt} = \frac{\partial}{\partial t} + v_i \frac{\partial}{\partial z} \tag{6}$$

To close equations (1)–(5), we need a gas equation of state relating pressure and density, and constitutive relations for the gas-particle and particle-particle interaction forces I_{gi} and I_{ji}. We assume that gas density follows the ideal gas law

$$\rho_g = \frac{p m_g}{RT} \tag{7}$$

in which m_g is the gas molar mass, R is the gas constant, and T is the temperature, which is assumed to be constant (given the thermal inertia and buffering of the solid particles) [see *Bercovici and Michaut*, 2010].

Following *Bercovici and Michaut* [2010], we assume that gas-particle interaction forces can be divided into two parts: steady state drag due to viscous laminar and turbulent flow of the gas and unsteady force due to acceleration of the relative velocity in the form of virtual mass (added mass) effect. We also assume that the drag force in a polydisperse system is equal to the monodispersed drag force; i.e.,

$$I_{gi} = c_i \varphi_i \left(1 + \Gamma_i \rho_g |\Delta v_i|\right) \Delta v_i + A \frac{1}{2} \breve{\rho}_i \left(\frac{\partial \Delta v_i}{\partial t} + \breve{v}_i \frac{\partial \Delta v_i}{\partial z}\right) \tag{8}$$

where for particle motion through a mixture of gas and other particles, the drag coefficients depend on gas viscosity μ and particle radius r_i as follows [*Bercovici and Michaut*, 2010]:

$$c_i = 3\mu / r_i^2, \quad \Gamma_i = r_i / \mu \tag{9}$$

Relative particle velocity $\Delta v_i = v_i - v_g$ and effective interface density and velocity

$$\breve{\rho}_i = \frac{\rho_g \rho_m \varphi_g \varphi_i}{\rho_m \varphi_g + \rho_g \varphi_i} \tag{10}$$

$$\breve{v}_i = \frac{\rho_m \varphi_g v_i + \rho_g \varphi_i v_g}{\rho_m \varphi_g + \rho_g \varphi_i} \tag{11}$$

are introduced here [see *Bercovici and Michaut*, 2010]. Various expressions for drag coefficients c_i and Γ_i were proposed in the literature [*Beetstra et al.*, 2007; *Crowe et al.*, 1998; *Hill et al.*, 2001; *Nigmatulin*, 1991]. In general,

©2015. The Authors.

these coefficients also depend on Reynolds number, volume concentration of particles, and some other parameters. However, while more complicated models for these parameters add complexity to the expressions (9), they are still based on the simplifying assumptions about particles shape and arrangement. There is even more uncertainty with the particle-particle drag force I_{ji} for which only limited data exist [*Holloway et al.*, 2010; *Yin and Sundaresan*, 2009]. We leave the full accounting of these forces for future work and assume that the volume concentration of particles is small, and thus, the particle-particle interaction force is much smaller than gas-particle interaction. Indeed, analysis of volcanic pumice suggests that magma fragmentation occurs at $\varphi = 77\,\%$ [*Woods*, 1995], at which point solid fragments become highly dispersed and effectively noninteracting.

3. One-Dimensional Acoustic Waves

Explosive gas release during volcanic eruptions produces small amplitude pressure perturbations that may be detected by microphones and seismometers as seismic or acoustic waves, depending on whether they travel through the air or through bedrock. Specific features of these waves can give important information on the eruptive mechanism, dynamics of explosion, source of the volcanic tremor, physical properties of magmatic fluids, and so on [*Bercovici et al.*, 2013; *Chouet*, 2003; *Jellinek and Bercovici*, 2011; *Johnson et al.*, 2004; *Vergniolle et al.*, 1996]. In order to interpret seismic or acoustic data a model that relates acoustic properties to the processes in a volcano is needed. Often acoustic waves are studied in a pseudogas approximation which assumes that gas and suspended particles move with the same velocity [*Drew and Passman*, 1999]. Phase separation in two-phase flows significantly alters the propagation pattern of acoustic waves leading to their dispersion and attenuation [*Bercovici and Michaut*, 2010; *Nigmatulin*, 1991]. The presence of more than one dispersed phase results in additional phenomena such as the dependence of the dispersion relation on interaction forces and physical properties, volume fraction, and size distribution of particles [*Gubaidullin and Nigmatulin*, 2000; *Gubaidullin et al.*, 2011; *Ishii and Matsuhisa*, 1983]. The accuracy of the "one-particle size" approximation depends on the actual size distribution function and reduces with increasing standard deviation. Much of the previous work on acoustic wave propagation in multiphase media has been concerned with gas-water vapor systems representing fogs or dusty gas. Here we study the effect of particle size distribution on the properties of plane acoustic waves in a volcanic conduit using a simplified model of a polydisperse suspension. We linearize the system of equations by considering small perturbations to a steady state, which we denote with a subscript "0" according to

$$\begin{aligned} \varphi_g &= \varphi_{g0} + \varepsilon\varphi_{g1} \\ \varphi_i &= \varphi_{i0} + \varepsilon\varphi_{i1} \\ v_g &= \varepsilon v_{g1} \\ v_i &= \varepsilon v_{i1} \\ \rho_g &= \rho_0(1 + \varepsilon\theta) \end{aligned} \tag{12}$$

where ε is a small parameter. The 0th order steady state is assumed uniform, which corresponds to the zero-gravity assumption; in this case the 0th order velocity is the same for all phases, and we therefore represent the system in the frame of reference traveling with the flow (thereby removing the 0th order velocity) [see *Bercovici and Michaut*, 2010]. Substitution of equations (12) into (1)–(5) and (8) leads to the linearized governing equations

$$\frac{\partial\varphi_{g1}}{\partial t} + \varphi_{g0}\frac{\partial\theta}{\partial t} + \varphi_{g0}\frac{\partial v_{g1}}{\partial z} = 0 \tag{13}$$

$$\frac{\partial\varphi_{i1}}{\partial t} + \varphi_{i0}\frac{\partial v_{i1}}{\partial z} = 0 \tag{14}$$

$$\varphi_{g0}\rho_0\frac{\partial v_{g1}}{\partial t} = -C_g^2\varphi_{g0}\rho_0\frac{\partial\theta}{\partial z} + \sum_{i=1}^{m}\left(c_i\varphi_{i0}\Delta v_{i1} + \breve{\rho}_{i0}\frac{A}{2}\frac{\partial v_{i1}}{\partial t}\right) \tag{15}$$

$$\varphi_{i0}\rho_m\frac{\partial v_{i1}}{\partial t} = -C_g^2\varphi_{i0}\rho_0\frac{\partial\theta}{\partial z} - c_i\varphi_{i0}\Delta v_{i1} - \frac{A}{2}\breve{\rho}_{i0}\frac{\partial v_{i1}}{\partial t} \tag{16}$$

where $C_g = \sqrt{RT/m_g}$ is the gas sound speed, $\Delta v_{i1} = v_{i1} - v_{g1}$ is a linearized separation velocity of phase i ($i = 1, 2 \ldots, m$), and $\breve{\rho}_{i0}$ is given by equation (10) (evaluated for $\varphi_g = \varphi_{g0}$, $\varphi_i = \varphi_{i0}$, and $\rho_g = \rho_0$). Note that turbulent drag term does not enter the linearized equations (13)–(16) and thus does not influence the propagation of sound waves in a mixture. Substituting the linearized gas and solid velocities v_{g1} and v_{i1} with

©2015. The Authors.

the separation velocity Δv_{i1} and mean velocity $\overline{v} = v_{g1}\varphi_{g1} + \sum_{i=1}^{m} v_{i1}\varphi_{i1}$, equations (13)–(16) can be rewritten in the form

$$\varphi_{g0}\frac{\partial\theta}{\partial t} + \frac{\partial\overline{v}}{\partial z} = 0 \tag{17}$$

$$\frac{\partial\theta}{\partial t} - \frac{\partial\Delta v_{i1}}{\partial z} + \frac{1}{\varphi_{g0}}\frac{\partial\varphi_{g1}}{\partial t} - \frac{1}{\varphi_{i0}}\frac{\partial\varphi_{i1}}{\partial t} = 0 \tag{18}$$

$$\overline{\rho}_0\frac{\partial\overline{v}}{\partial t} + \Delta\rho_0\varphi_{g0}\sum_{i=1}^{m}\varphi_{i0}\frac{\partial v_{i1}}{\partial t} = -\rho_0 C_g^2\frac{\partial\theta}{\partial z} \tag{19}$$

$$\varphi_{g0}\Delta\rho_0\frac{\partial\overline{v}}{\partial t} + \widetilde{\rho}_i\frac{\partial\Delta v_{i1}}{\partial t} + \sum_{j=1}^{m}\hat{\rho}_j\frac{\partial\Delta v_{j1}}{\partial t} = -c_i\varphi_{g0}\Delta v_{i1} - \sum_{j=1}^{m} c_j\varphi_{j0}\Delta v_{j1} \tag{20}$$

where

$$\widetilde{\rho}_i = \varphi_{g0}\left(\rho_m + \frac{A}{2}\frac{\breve{\rho}_{i0}}{\varphi_{i0}}\right) \tag{21}$$

$$\hat{\rho}_j = \frac{A}{2}\breve{\rho}_{j0} - \varphi_{g0}\varphi_{j0}\Delta\rho_0 \tag{22}$$

$$\overline{\rho}_0 = \varphi_{g0}\rho_0 + \left(1 - \varphi_{g0}\right)\rho_m \tag{23}$$

$$\Delta\rho_0 = \rho_m - \rho_0 \tag{24}$$

Equation (17) is a result of the summation of equations (14) over all m solid phases divided by ρ_m and equation (13) divided by ρ_0. For each solid phase i ($i = 1, 2, \ldots m$), equation (18) was obtained by subtraction of (14) divided by $\rho_m\varphi_{i0}$ from (13) divided by $\rho_0\varphi_{g0}$. Equation (19) arises from the summation of m equations (16) and (15). The subtraction of (16) multiplied by φ_0/φ_{i0} from (15) gives equation (20). In the limit when only one solid phase is present these equations coincide with equations (21)–(25) from *Bercovici and Michaut* [2010]. The complete system of governing equations is thus (3) and (17)–(20).

4. Dispersion Relation

In this section, we look at normal modes and for simplicity consider only a straight conduit (c.f. *Fee et al.* [2010b] for an example of variable conduit width). We seek solutions to equations (3) and (17)–(20) in the form of traveling plane waves so that

$$\left(\theta, \overline{v}, \Delta v_{i1}, \varphi_{g1}, \varphi_{i1}\right) \sim \exp(ikz - i\omega t) \tag{25}$$

where k is the wave number and ω is the angular frequency. The dispersion relation between the wave number and frequency can be obtained by substituting (25) into the governing equations and then finding the conditions for the existence of a nontrivial solution. In general, both wave number k and frequency ω can be complex numbers; their imaginary parts represent spatial and temporal attenuation or growth, respectively. For wave propagation in a finite domain, wherein time-varying boundary conditions are prescribed, the frequency is assumed real, the wave number is complex, and the attenuation or growth with distance is given by $\Im(k)$ [*Bourbié*, 1987]. If, on the other hand, waves propagate through an unbounded domain, then only initial conditions are prescribed; in this case, the wave number is real, and the complex part of the frequency gives wave decay or growth with time [*Edelman*, 2004; *Lopatnikov and Cheng*, 2004]. Regardless of setting, it is often convenient to replace the frequency in equation (25) with the wave speed according to $C = \omega/k$. Here we consider propagation of waves in an unbounded conduit. We introduce a ratio of magma and gas densities $\beta = \rho_m/\rho_0$, the nondimensional wave speed $\hat{C} = C/C_g$, and nondimensional wavelength $\lambda_i = c_i/(kC_g\rho_0)$, which varies as the inverse of the particle size and accounts for the attenuation due to gas drag.

©2015. The Authors.

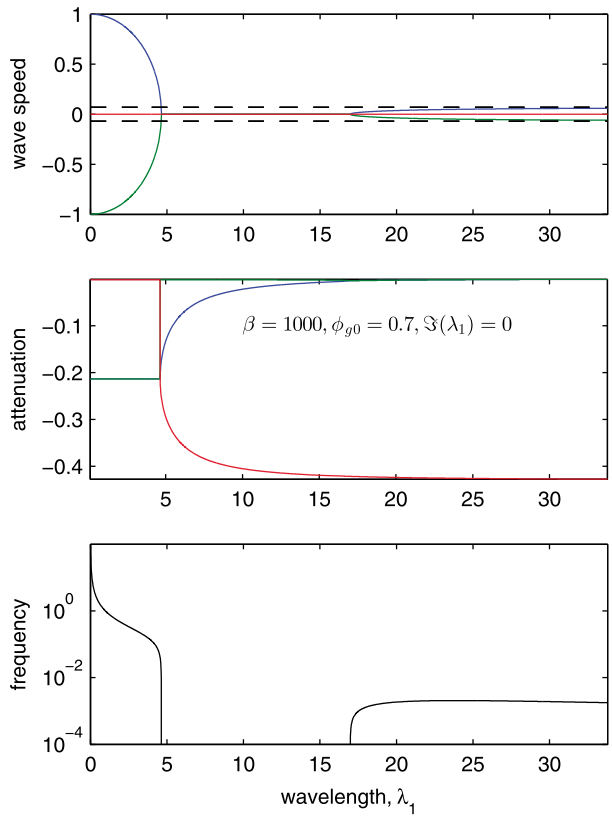

Figure 1. Nondimensional wave speed, temporal attenuation (decay rate), and frequency of acoustic waves in a two-phase mixture. Three solutions to characteristic equation (26) are shown; green and blue lines represent upward and downward propagating waves, respectively, while the red curve indicates the purely imaginary nonpropagating solution. Dashed lines indicate the pseudogas sound speed.

4.1. Two-Phase System

We start with the simplest case of magma particles of a single size, which leads us to the basic two-phase gas-particle formulation. The dispersion relation takes the form

$$\hat{C}^3\varphi_{g0}^2\beta\left(\frac{A}{2}\gamma_2+\gamma_1\right)+i\hat{C}^2\varphi_{g0}\lambda_1\gamma_1\gamma_2 - \hat{C}\varphi_{g0}\left(\frac{A}{2}\beta+\gamma_1^2\right)-i\lambda_1\gamma_1=0 \qquad (26)$$

where

$$\gamma_1 = 1+(\beta-1)\varphi_{g0}$$
$$\gamma_2 = \beta-(\beta-1)\varphi_{g0}$$

This equation with slightly different notations was given by *Bercovici and Michaut* [2010]; it is a cubic equation in wave speed $\hat{C}$ and linear in wavelength λ_1. The solutions to this equation, for $\varphi_{g0}=0.7$, $\beta=1000$, and in the absence of spatial attenuation ($\Im(\lambda_1)=0$), are presented in Figure 1. There are two nontrivial solutions, corresponding to upward and downward propagating plane waves marked by green and blue lines. The third solution is solely imaginary (red line). The nontrivial solutions exhibit three different modes. For small wavelength, the phase velocity of either upward or downward propagating waves is much higher than the pseudogas sound speed $C_\psi = C_g\sqrt{\rho_0/\left(\varphi_{g0}\bar{\rho}_0\right)}$ (see Figure 1, dashed line). In the limit of very small wavelengths and very weak drag ($\lambda_1\to 0$), the waves effectively travel through the gas with little particle motion and thus propagate at almost the pure gas sound speed. The values at short wavelength are highest that the wave speed can reach in a two-phase mixture. With increasing wavelength, the drag due to relative motion of gas and particles is large enough to cause overdamping of acoustic waves and the sound speed reduces rapidly to zero, at which point it reaches a range of λ_1 for which $\Re(\hat{C})=0$; i.e., waves do not propagate or are entirely attenuated and blocked. The existence of nonpropagating waves was also predicted for poroelastic materials in certain frequency ranges [*Lopatnikov and Cheng*, 2004]. Beyond this pure-attenuation or "mute" range of wave numbers, at higher values of λ_1, acoustic waves emerge again. However, the gas drag is large and/or particle size is very small so that the gas and solid particles are effectively locked together and form a dusty gas mixture. In such mixtures, waves are slow and attenuation due to relative particle motion in the gas is small. The width of each zone in wavelength space depends on the density ratio β and initial gas volume fraction φ_{g0} (see *Bercovici and Michaut* [2010] for details). The dimensionless frequencies $\hat{\omega}=\Re\left(\hat{C}/\lambda_1\right)$ of fast and slow waves are distinct from each other. Fast waves have a wide spectrum of high frequencies (from 0.01 up to 100 in Figure 1), while slow waves are shifted toward lower frequencies ranging from 2×10^{-4} to 2.05×10^{-3} and exhibit a peak frequency of $\hat{\omega}=2.05\times10^{-3}$ at $\lambda_1=24$ (see Figure 1). Frequencies between 2.05×10^{-3} and 10^{-2} are blocked. Figure 2 shows dispersion relations in a gas-ash mixture with two different solid particle fractions. The increasing fraction of ash narrows the domain in which fast waves with small wavelengths exist. These fast waves are more strongly attenuated than are the slow waves at large wavelength, and the larger the volume fraction of solid particles the greater the attenuation. At very long wavelength, the waves become virtually nondissipative.

©2015. The Authors.

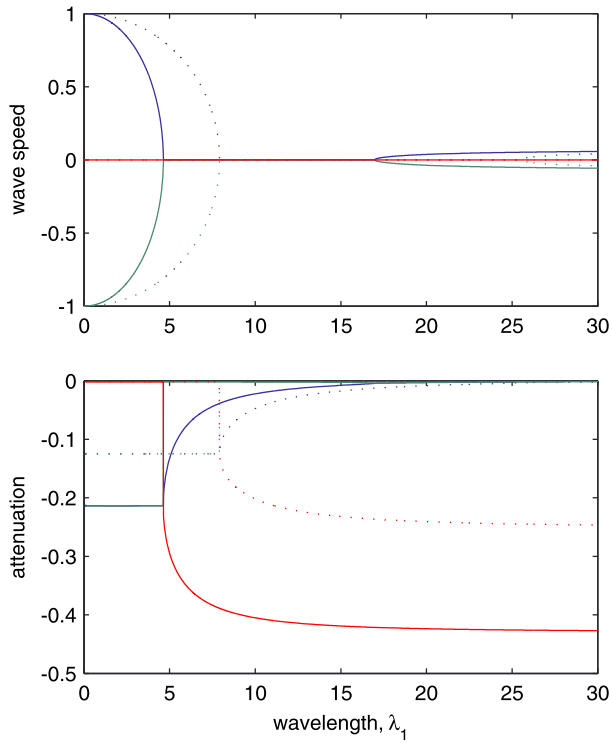

Figure 2. Dependence of wave speed and attenuation on gas volume fraction in a two-phase mixture. Two different cases are shown: solid lines correspond to $\varphi_{g0} = 0.7$ and dashed lines correspond to $\varphi_{g0} = 0.8$. All other parameters are kept the same as in Figure 1 ($\beta = 1000$, $\Im(\lambda_1) = 0$).

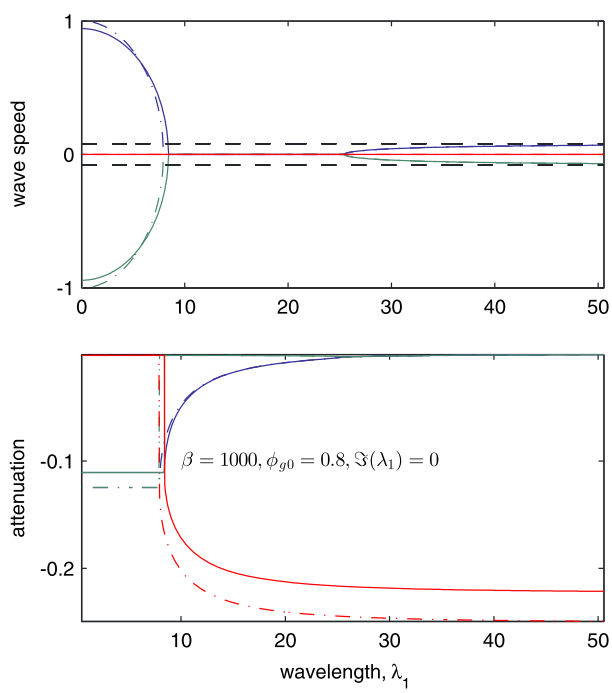

Figure 3. Influence of inertial exchange (or added mass force) between the phases on acoustic wave speed and attenuation. Solid lines reflect dispersion relation that accounts for added mass force ($A = 1$), and broken lines show solution without inertial exchange ($A = 0$).

Here the 0th order steady state is assumed uniform, which corresponds to the zero-gravity assumption. *Bercovici and Michaut* [2010] considered acoustic waves in a gravitationally separating column. They show that propagation of acoustic waves is only very slightly dependent on the presence of gravity. Three distinct acoustic modes are preserved during stratification. Fast waves at short wavelength and pseudogas waves at long wavelength are essentially identical to those in a zero-gravity limit. The third purely imaginary nonpropagating mode transforms into very slow porosity wave that in the presence of gravity travels with the separation velocity. *Bercovici and Michaut* [2010] also show that for the typical values of parameters ($\rho_m \approx 2500$ kg m^{-3}, 2 kg m$^{-3} \le \rho_g \le 30$ kg m^{-3}, and $0.7 \le \varphi_g \le 0.99$ from the top to the bottom of the column and $C_g \approx 700$ m s^{-1}) acoustic waves feel little effect of the background gradients over increments in height under 1000 m.

Before proceeding to a more complicated system with particles of different sizes, we examine how inertial exchange between the phases affects the propagation of sound waves and at which conditions it can be ignored. Figure 3 shows solution to dispersion relation (26) with ($A = 1$) and without ($A = 0$) the added mass force at $\beta = 1000$ and $\varphi_{g0} = 0.8$. Two solutions follow each other very closely at low-volume fractions of suspended particles. The effect of the added mass force on wave propagation is most profound at low λ_1 where it slightly reduces wave speed and increases attenuation. This force also slightly reduces the range of λ_1 at which waves are blocked. The difference between two solutions increases slightly with increasing density ratio β and particles volume fraction. However, its effects at the low-volume fractions of suspended particles (as studied here) are insignificant and therefore can be safely neglected. Another simplifying assumption of this

©2015. The Authors.

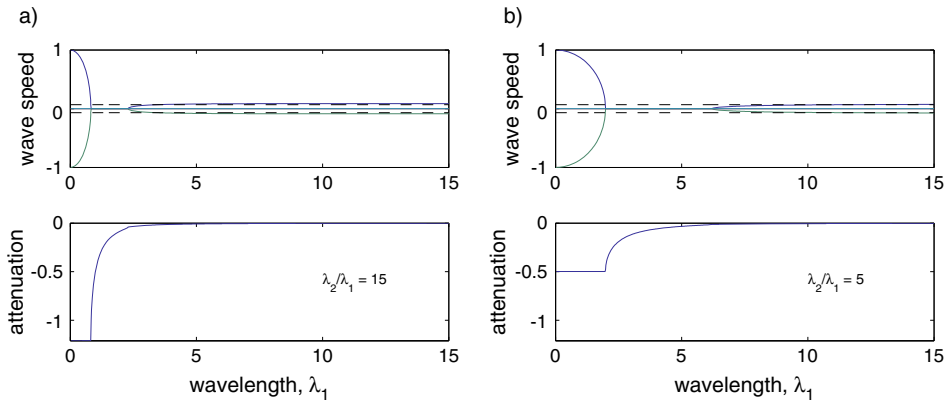

Figure 4. (a and b) Nondimensional wave speed and attenuation factor for acoustic wave in a volcanic eruption with binary distribution of particle sizes. All four solutions to characteristic equation (29) are shown by different colors. Two purely imaginary solutions are marked with cyan color; blue and green colors correspond to upward and downward propagating waves. Calculations were performed for $\beta = 1000$, $\varphi_{g0} = 0.7$, $\varphi_{10} = 0.2$, and $\varphi_{20} = 0.1$.

study is negligible particle-particle and wall drags. For gas-pyroclastic flows after fragmentation, particle-particle drag can be represented in the form

$$I_{ji} = F\left(\varphi_i, \varphi_j, r_i, r_j, \rho_s\right)\left|v_j - v_i\right|\left(v_i - v_j\right) \tag{27}$$

where F is a certain function of particle volume fractions, particle sizes, and densities [*Neri et al.*, 2003] and the wall drag can be written [*Kozono and Koyaguchi*, 2009b; *Vergniolle and Jaupart*, 1986] as

$$\begin{aligned} I_{gw} &= \frac{\lambda}{4r_c}\rho_g v_g^2 \operatorname{sgn}\left(v_g\right), \quad \text{for gas phase} \\ I_{iw} &= 0, \quad \text{for dispersed phase} \end{aligned} \tag{28}$$

where r_c is the conduit radius and λ is a friction coefficient. Note that the friction coefficient is essentially independent of the number of solid phases and the particle size. One can see that equations (13)–(17) driving acoustic waves contain only linear parts of the drag forces. Thus, the nonlinear components of drag given by equations (27) and (28) do not influence the propagation of acoustic waves, which are linear disturbances.

4.2. Three-Phase System

When magma particles of two different sizes are present, the dispersion relation takes the form

$$\begin{aligned} &\hat{C}^4\varphi_{g0}^2\beta^2 + i\hat{C}^3\varphi_{g0}\beta(\lambda_1\gamma_4 + \lambda_2\gamma_5) - \hat{C}^2\varphi_{g0}(\lambda_1\lambda_2\gamma_2 + \beta\gamma_1) - \\ &-i\hat{C}[\beta(\lambda_1 + \lambda_2) - (\lambda_1\varphi_{20} + \lambda_2\varphi_{10})\gamma_3] + \lambda_1\lambda_2 = 0 \end{aligned} \tag{29}$$

where

$$\begin{aligned} \gamma_3 &= \beta + (\beta - 1)\varphi_{g0} \\ \gamma_4 &= \varphi_{g0} + \beta\varphi_{10} \\ \gamma_5 &= \varphi_{g0} + \beta\varphi_{20} \end{aligned}$$

In deriving (29), we follow the discussion at the end of the previous section and neglect the added mass force. We assume that $r_1 > r_2$; i.e., smaller particles are assigned the index 2. In case $r_1 = r_2$, (29) reduces to (26) with $A = 0$. For systems with a binary particle size distribution, there are four solutions to the dispersion relation. However, only two solutions are nontrivial and correspond to the upward and downward propagating waves, as with the case for the unary size distribution considered above. Even with the second population of particles, the main features of acoustic wave propagation are preserved (Figure 4). In particular, there are still three different regions in the wavelength domain that correspond to superfast propagating waves, the mute region in which acoustic waves do not propagate and a region where acoustic wave speed approaches the slow pseudogas limit. With the presence of two particle populations, the mute region shifts to the left and contracts (Figure 4). Moreover, as the ratio in particle sizes λ_2/λ_1 increases, the domain of fast short-wavelength waves also shrinks, and these waves become more attenuated. The proportions of the two different populations in the mixture also affect the wave speed and attenuation factor. Increasing the

©2015. The Authors.

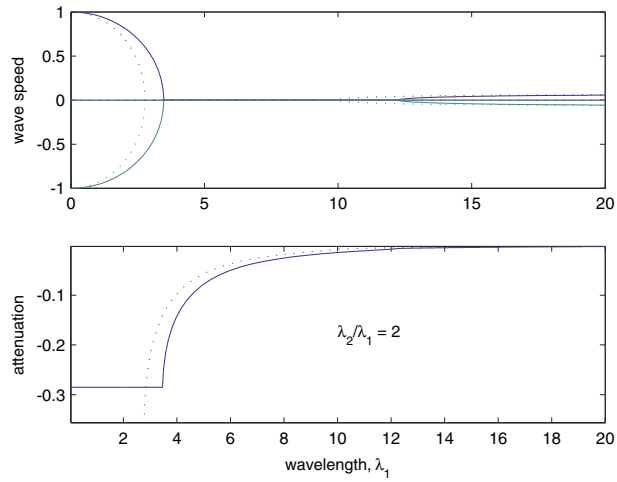

Figure 5. Wave speed and attenuation factor for two distributions of particles with different proportions of solid particles and the same values of all other parameters ($\varphi_{g0} = 0.7$, $\beta = 1000$, and $\lambda_2/\lambda_1 = 2$). Solid lines represent case when $\varphi_{10} = 0.2$ and $\varphi_{20} = 0.1$ while dotted lines indicate the reverse case when $\varphi_{10} = 0.1$ and $\varphi_{20} = 0.2$.

volume fraction of larger particles leads to a wider region of fast short-wavelength waves and reduces their attenuation relative to mixtures with identical particles (Figure 5). To examine the width of the regions with fast and blocked waves, we consider the limiting case when large particles are much bigger than small particles ($\lambda_2/\lambda_1 \to \infty$); the blocked region is defined by $\hat{C}$ being purely imaginary, and thus, we write $\hat{C} = -iC_i$. It follows from equation (29) that

$$\lambda_1 + \lambda_1 C_i^2 \gamma_2 \varphi_{g0} + C_i\left(\gamma_3\varphi_{10} - \beta - C_i^2\gamma_5\varphi_{g0}\beta\right) = 0 \tag{30}$$

Values of λ_1 for which solutions to (30) are real determine the mute region. $\hat{C}$ would be purely imaginary (C_i real) if the discriminant of the cubic equation (30) is zero [see *Bercovici and Michaut*, 2010], that is, if

$$4\lambda_1^4\gamma_2^3\varphi_{g0}^2 + \lambda_1^2\varphi_{g0}\left(27\gamma_5^2\beta^2 + 18\gamma_2\gamma_5\beta(\gamma_3\varphi_{10} - \beta) - \gamma_2^2(\gamma_3\varphi_{10} - \beta)^2\right) - 4\beta\gamma_5(\gamma_3\varphi_{10} - \beta)^3 = 0 \tag{31}$$

This equation is quadratic in λ_1^2, and it, in turn, has nonzero real roots if its own discriminant is nonnegative, i.e., when

$$8\beta\gamma_5 + \varphi_{10}\left(\gamma_2\gamma_3 - \beta^2\right) \le 0 \tag{32}$$

For example, for $\beta = 1000$ and $\varphi_{g0} = 0.7$, the inequality (32) gives limitations on the particle volume fractions at which mute region exists. So at $\varphi_{10} = 0.29$ and $\varphi_{20} = 0.01$ there is a range of λ_1 at which acoustic waves do not propagate but at $\varphi_{10} = 0.28$ and $\varphi_{20} = 0.02$ the mute region does not exist, and thus, all waves propagate, although the region of fast short-wavelength waves will be very narrow and limited to λ_1 close to zero.

4.3. Four-Phase System

The four-phase system consists of gas and magma particles of three different sizes. The characteristic equation for the sound speed (the solution of which yields the dispersion relation) in the absence of added mass forces becomes

$$\begin{aligned}
&\hat{C}^5\varphi_{g0}^2\beta^3 + i\hat{C}^4\varphi_{g0}\beta^2[\gamma_4\lambda_1 + \gamma_5\lambda_2 + \gamma_6\lambda_3] - \\
&-\hat{C}^3\varphi_{g0}\beta[\lambda_1\lambda_2(\gamma_2 - \varphi_{30}\beta) + \lambda_1\lambda_3(\gamma_2 - \varphi_{20}\beta) + \lambda_2\lambda_3(\gamma_2 - \varphi_{10}\beta) + \beta\gamma_1] + \\
&+i\hat{C}^2\beta\gamma_3[\lambda_1(\varphi_{20} + \varphi_{30}) + \lambda_2(\varphi_{10} - \varphi_{30}) + \lambda_3(\varphi_{10} - \varphi_{20})] - \\
&-i\hat{C}^2\left[\beta^2(\lambda_1 + \lambda_2 + \lambda_3) + \lambda_1\lambda_2\lambda_3\varphi_{g0}\gamma_2\right] + \\
&+\hat{C}[\lambda_1\lambda_2(\beta - \varphi_{30}\gamma_3) + \lambda_1\lambda_3(\beta - \varphi_{20}\gamma_3) + \lambda_2\lambda_3(\beta - \varphi_{10}\gamma_3)] + i\lambda_1\lambda_2\lambda_3 = 0
\end{aligned} \tag{33}$$

where

$$\gamma_6 = \varphi_{g0} + \beta\varphi_{30}$$

The dispersion relations for two- and three-phase mixtures follow from equation (33) in the limits when $\varphi_{20} = \varphi_{30} = 0$ and $\varphi_{30} = 0$, respectively. Although equation (33) has five roots, only two of them are nontrivial, as before. The behavior of wave speed and attenuation in a four-phase system is qualitatively similar to that of two- and three-phase systems. The role of the additional particle population lies in further shrinking the window of fast short-wavelength waves and in increasing their attenuation (Figure 6).

©2015. The Authors.

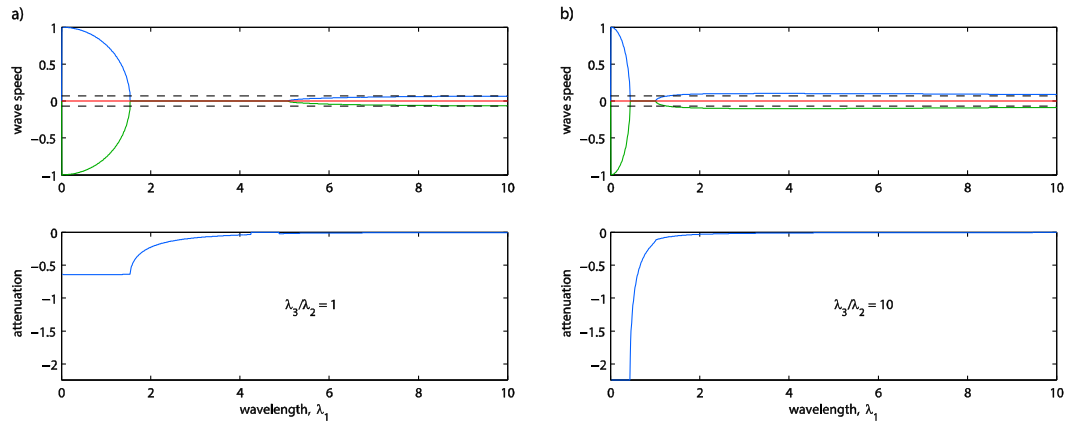

Figure 6. Dimensionless wave speed and attenuation in a four-phase system for two different ratios of particle sizes: $r_1^2 : r_2^2 : r_3^2 = 5:1:1$ and $r_1^2 : r_2^2 : r_3^2 = 50:10:1$ calculated at $\beta = 1000$, $\varphi_{g0} = 0.7$, $\varphi_{10} = 0.15$, $\varphi_{20} = 0.1$, and $\varphi_{30} = 0.05$.

4.4. High- and Low-Wavelength Asymptotics

One can readily demonstrate, using (26), (29), and (33), that particle size distribution in volcanic eruptions does not affect the asymptotic behavior of acoustic waves. In the limit $\lambda_1 = 0$ ($\lambda_2/\lambda_1 \to \infty$) and in the absence of the added mass effect, all three equations lead to

$$\hat{C}^2 = \frac{\gamma_1}{\varphi_{g0}\beta} = \frac{1 + (\beta - 1)\varphi_{g0}}{\varphi_{g0}\beta} \tag{34}$$

Thus, at small wavelengths, there are always fast propagating waves. As $\varphi_{g0} \to 1$ or $\beta \to \infty$, $\hat{C}^2 \to 1$; i.e., the wave speed approaches sound speed of pure gas. With the added mass effect, however, the limit $\beta \to \infty$ ($\rho_m \gg \rho_0$) leads instead to

$$\hat{C}^2 \to \frac{2\varphi_{g0}}{1 + \varphi_{g0}} \tag{35}$$

which implies that the added mass effect reduces the wave speed slightly. In the limit of very large wavelength ($\lambda_1 \to \infty$), equations (26), (29), and (33) give

$$\hat{C}^2 = 1/\left(\gamma_2 \varphi_{g0}\right) = C_\psi^2 / C_g^2 \tag{36}$$

which again means that long-wavelength waves travel with the pseudogas sound speed.

5. Choking and Size Distribution

The choking condition for compressible conduit flows is an important problem in volcanological research since it provides constraints on the maximum eruption velocity in a simple straight conduit. (Supersonic velocities can be achieved for special conduit geometries, or as the erupting gas exits into colder ambient atmosphere.) In particular, once a flow reaches its material's sound speed, no pressure change inside or outside the conduit can increase the velocity; hence, it is "choked" at the sound speed. Choking is associated with a discontinuity in gradients of mixture properties, since material downstream of any fluid moving at the sound speed is impervious to the impinging flow (since pressure cannot be propagated downstream faster than the flow itself), and thus, there is zero adjustment length for this material. Thus, determining the conditions for this shock or discontinuity in our system provides the choking condition [see *Bercovici and Michaut*, 2010; *Kozono and Koyaguchi*, 2009a, 2009b; *Vergniolle and Jaupart*, 1986].

5.1. Nonlinear Steady State With Size Distribution

Nonlinear steady state solutions to the governing equations (1)–(7) can be obtained by assuming that all time derivatives $\partial/\partial t = 0$. We also assume that at the fragmentation point, $z = 0$, all phases have the same velocity

©2015. The Authors.

$v_g = v_i = W_0$ and that $\rho_g = \rho_0$, $\varphi_g = \varphi_{g0}$, and $\varphi_i = \varphi_{i0}$. In this case mass conservation requires

$$v_g = \frac{\varphi_{g0} W_0}{\theta \varphi_g}, v_i = \frac{\varphi_{i0} W_0}{\varphi_i} \tag{37}$$

where $\theta = \rho_g/\rho_0$. Substitution of (36) and $z = \left(W_0^2/g\right)z'$ into the momentum equations leads to

$$\frac{d}{dz}\frac{\varphi_{g0}}{\theta\varphi_g} = -\overline{\alpha}^2 \frac{\varphi_g}{\varphi_{g0}}\frac{d\theta}{dz} - \theta\frac{\varphi_g}{\varphi_{g0}} + \sum_{i=1}^{m}\frac{\varphi_{i0}}{\varphi_{g0}}\Delta L_i \tag{38}$$

$$\frac{d}{dz}\frac{\varphi_{i0}\beta}{\varphi_i} = -\overline{\alpha}^2 \frac{\varphi_i}{\varphi_{i0}}\frac{d\theta}{dz} - \beta\frac{\varphi_i}{\varphi_{i0}} - \Delta L_i \tag{39}$$

where we drop the prime on z' after the necessary substitutions. The following notations are used here

$$\Delta L_i = D_i \Delta U_i \tag{40}$$

$$D_i = \frac{\varphi_i}{\varphi_{i0}}\left(D_i^0 + D_i^\tau \theta |\Delta U_i|\right) \tag{41}$$

$$\Delta U_i = \frac{\Delta v_i}{W_0} = \frac{\varphi_{i0}}{\varphi_i} - \frac{\varphi_{g0}}{\varphi_g} \tag{42}$$

with $\overline{\alpha} = C_g/W_0$, $D_i^0 = \frac{W_0 c_i}{g\rho_0}$, and $D_i^\tau = \frac{3W_0^2}{g r_i}$.

5.2. Choking Conditions

Across a choking point flow decelerates because the external pressure does not adjust to the increases in internal pressure. This leads to transition from $dv_g/dz > 0$ in the conduit to $dv_g/dz < 0$ across the shock. Thus, a choked flow criterion can be established from (38) and (39) by inferring the conditions at which the gradients of the gas density and volume fractions of components undergo discontinuous changes, i.e., when $d\theta/dz$, $d\varphi_g/dz$, and $d\varphi_i/dz$ become singular. For that, we rewrite equations (38) and (39) in the following form

$$\left(\overline{\alpha}^2\frac{\varphi_g}{\varphi_{g0}} - \frac{1}{\theta^2}\frac{\varphi_{g0}}{\varphi_g}\right)\frac{d\theta}{dz} + \frac{\varphi_{g0}}{\theta\varphi_g^2}\sum_{i=1}^{m}\frac{d\varphi_i}{dz} = -\theta\frac{\varphi_g}{\varphi_{g0}} + \sum_{i=1}^{m}\frac{\varphi_{i0}}{\varphi_{g0}}\Delta L_i \tag{43}$$

$$\frac{\varphi_{i0}\beta}{\varphi_i^2}\frac{d\varphi_i}{dz} = \overline{\alpha}^2\frac{\varphi_i}{\varphi_{i0}}\frac{d\theta}{dz} + \beta\frac{\varphi_i}{\varphi_{i0}} + \Delta L_i \tag{44}$$

After substituting $d\varphi_i/dz$ with $d\theta/dz$ from (44) equation (43) becomes

$$\left(\overline{\alpha}^2\frac{\varphi_g}{\varphi_{g0}} - \frac{1}{\theta^2}\frac{\varphi_{g0}}{\varphi_g} + \frac{\overline{\alpha}^2}{\beta}\frac{\varphi_{g0}}{\theta\varphi_g}\sum_{i=1}^{m}\frac{\varphi_i^3}{\varphi_g\varphi_{i0}^2}\right)\frac{d\theta}{dz} = -\theta\frac{\varphi_g}{\varphi_{g0}} - \frac{\varphi_{g0}}{\theta\varphi_g^2}\sum_{i=1}^{m}\left(\frac{\varphi_i^3}{\varphi_{i0}^2} + \Delta L_i\left(\frac{\varphi_i^2}{\varphi_{i0}\beta} - \theta\frac{\varphi_g^2\varphi_{i0}}{\varphi_{g0}^2}\right)\right) \tag{45}$$

A singularity in the last equation occurs when the bracketed factor on the left-hand side vanishes, i.e., when

$$\theta^2\frac{\varphi_g^2}{\varphi_{g0}^2} + \frac{\theta}{\beta}\sum_{i=1}^{m}\frac{\varphi_i^3}{\varphi_g\varphi_{i0}^2} = \frac{1}{\overline{\alpha}^2} \tag{46}$$

Equation (46) serves as a choking criterion, and the solution to the quadratic equation gives the nondimensional gas density θ at the choking point. The precise form of the solution $\theta(\varphi_g)$ is influenced by the gas-particle density ratio β, the ratio of the pure gas sound speed and the initial magma ascent velocity $\overline{\alpha}$, the initial gas volume fraction φ_{g0}, and the size distribution of solid particles. The choking relation changes, depending on the number of total phases assumed.

As we know from the previous research [*Bercovici and Michaut*, 2010], in the pseudogas limit, when $v_g = v_i$ $(i = 1, 2, \ldots, m)$ choking occurs at the critical gas density

$$\theta_c = \frac{1}{\overline{\alpha}}\sqrt{\varphi_{g0}\left(\beta\left(1-\varphi_{g0}\right) + \varphi_{g0}\right)} \tag{47}$$

and critical porosity

$$\varphi_c = \frac{\varphi_{g0}}{\theta_c\left(1-\varphi_{g0}\right) + \varphi_{g0}} \tag{48}$$

©2015. The Authors.

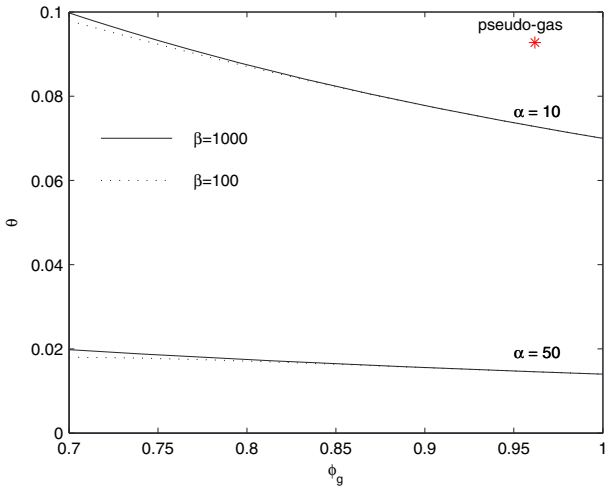

Figure 7. Choking criterion for a two-phase mixture at various values of $\overline{\alpha}$ and β ($\varphi_{g0} = 0.7$). The red star indicates the choking point for the pseudogas mixture.

For the two-phase mixture, choking might occur at any gas volume fraction, provided the gas reaches sufficient depressurization and low density (Figure 7). In that sense the choking condition depends on various parameters. For example, as the density ratio β increases, choking occurs at larger θ, i.e., with less depressurization. Moreover, the initial magma input velocity, characterized by the dimensionless parameter $\overline{\alpha}$, has a very strong influence on the choking criterion. For initial velocities in the range 5 m/s $\leq W_0 \leq$ 5 m/s, the parameter $\overline{\alpha}$ goes from 10 at high velocity to 100 at low velocity. Smaller $\overline{\alpha}$ (larger W_0) leads to choking for larger θ, i.e., with less depressurization. As a rule, the gas density at the choking point is lower than that in the pseudogas limit. However, at small values of $\overline{\alpha}$ (high initial magma velocities) the gas density at the choking point can be higher than that in the pseudogas limit. For $\overline{\alpha} = 10$, the pseudogas is less dense at $\varphi_g < 0.754$ (Figure 7). If choking occurs at very high gas fractions, the associated gas density in the two-phase system is less than that in the pseudogas mixture.

The presence of one more solid phase alters the choking criterion by making it depend on the volume fractions of solids. These effects are most pronounced if the flow chokes at low values of φ_g close to initial gas volume fraction φ_{g0} (Figure 8). For two solid phases of different particle sizes, the second solid phase reduces the gas density associated with choking; i.e., it delays the choking event to greater heights. However, as φ_g increases, the choking conditions for two- and three-phase mixtures converge on a single criterion.

In this study, we ignore the particle-particle drag, I_{ji}, and the wall drags, I_{gw} and I_{iw}. The analysis of choking is unaffected by introduction of these forms of drag given by equations (27) and (28), since the choking condition for the multiphase mixture (46) does not depend on drag. Introduction of the particle-particle and wall drag forces, however, might affect the height at which choking occurs and choking velocities. Nevertheless, the effects of these drag forces are expected to be of secondary importance in comparison to fluid-particle drag given the order of magnitude comparison of these forces. In general, particle-particle interaction is important for dense granular flows. However, theoretical studies show that even in the dense mixtures with a particle volume fraction up to 0.4 the particle-particle drag is at least 1 order of magnitude less than fluid-particle drag [*Yin and Sundaresan*, 2009] and is almost 2 orders of magnitude less for solid volume fractions ≈ 0.1. We focus on the dynamics of the flow in the conduit where gas volume fraction was shown to vary between 0.77 at the fragmentation point to close to 1 when gas expands rapidly near the vent. At these porosity ranges, direct particle-particle interaction (such as collision and breakup) is much less. *Wilson et al.* [1980] and *Bercovici and Michaut* [2010] showed that wall friction has a small effect on eruption velocities.

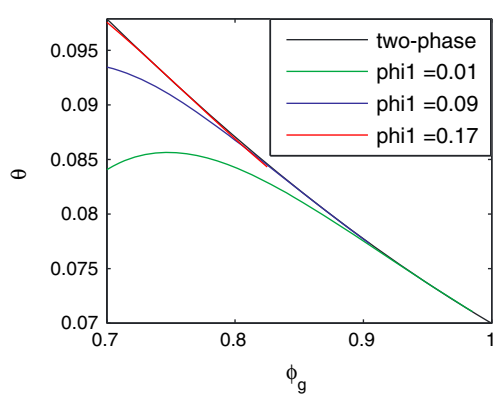

Figure 8. Choking criterion for a three-phase mixture. The black line shows the reference two-phase curve, while the three other curves show $\theta - \varphi_g$ critical relationship for various combinations of solid volume fractions φ_1 and φ_2. All calculations are for $\varphi_{g0} = 0.7$, $\varphi_{10} = 0.2$, $\beta = 100$, and $\overline{\alpha} = 10$.

©2015. The Authors.

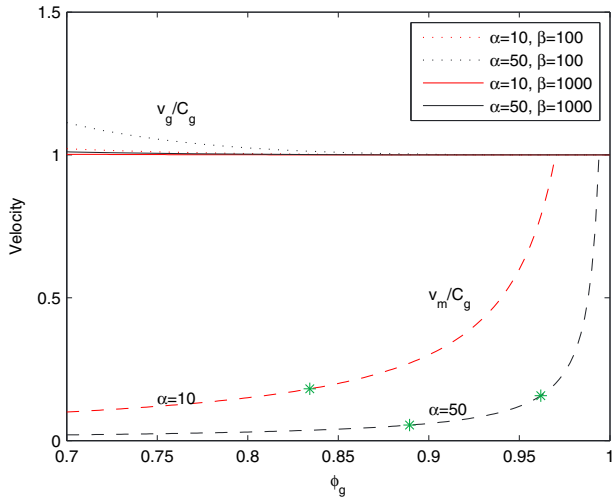

Figure 9. Choking velocities in a two-phase mixture. Parameters are the same as in Figure 7. Solid line is for the nondimensional gas velocity at $\beta = 1000$, while the dotted line is for $\beta = 100$. Colors distinguish different values of $\overline{\alpha}$ (red is for $\overline{\alpha} = 10$ and black is for $\overline{\alpha} = 50$). Green stars represent the pseudogas choking velocity (higher values of β lead to lower values of velocity), while the dashed lines show the nondimensional velocity of magma particles.

5.3. Choking Velocities

The choking criterion (46) can be reformulated in terms of fluid and solid velocities. The combination of equations (37) and (46) yields

$$\frac{\varphi_g}{\rho_g v_g^2} + \sum_{i=1}^{m} \frac{\varphi_i}{\rho_m v_i^2} = \frac{\varphi_g}{\rho_g C_g^2} = \frac{1}{\overline{\rho} C_\psi} \quad (49)$$

For single-phase flow ($\varphi_g = 1$, $\varphi_i = 0$) equation (49) reduces to the classical choking criterion, according to which the critical velocity is equal to the speed of sound. For multiphase flows, the choking velocity is a weighted average of particle and gas velocities.

In the pseudogas limit (46) holds, and the choking velocity is

$$v_g = v_i = \frac{1 - \varphi_{g0}}{1 - \varphi_g} W_0 \quad (50)$$

Note that in this approximation the gas and solid are ejected with the same velocity, which depends on initial gas volume fraction φ_{g0}, bulk velocity W_0, gas-particle density ratio β, and the pure gas sound speed C_g (from equation (47)).

In a two-phase mixture, the solid particles and gas separate. The exit velocity of the solid particles is fully determined by the fragmentation velocity and the gas volume fraction at the fragmentation and exit points

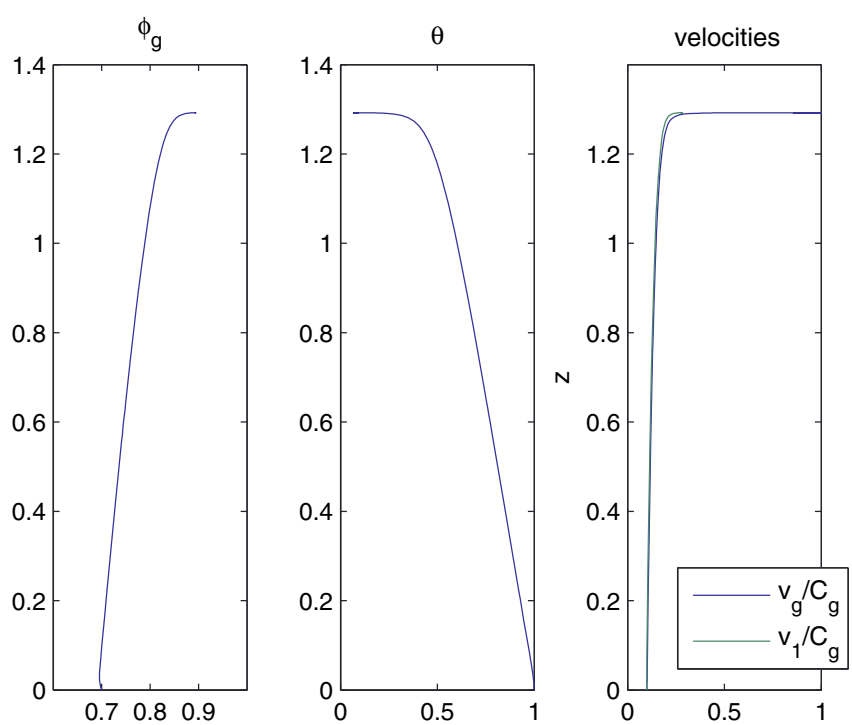

Figure 10. Example of the full solution of the nonlinear steady state equations for two-phase system obtained for $\overline{\alpha} = 10$, $\beta = 100$, $\varphi_{g0} = 0.7$, $D_1^0 = 1$, and $D_1^\tau = 10^5$. Notice that at high values of drag coefficient used for these calculations the solid particle velocity follows closely the gas velocity and at the choking point at $z = 1.29$ v_m is only 3.5 times less then v_g.

©2015. The Authors.

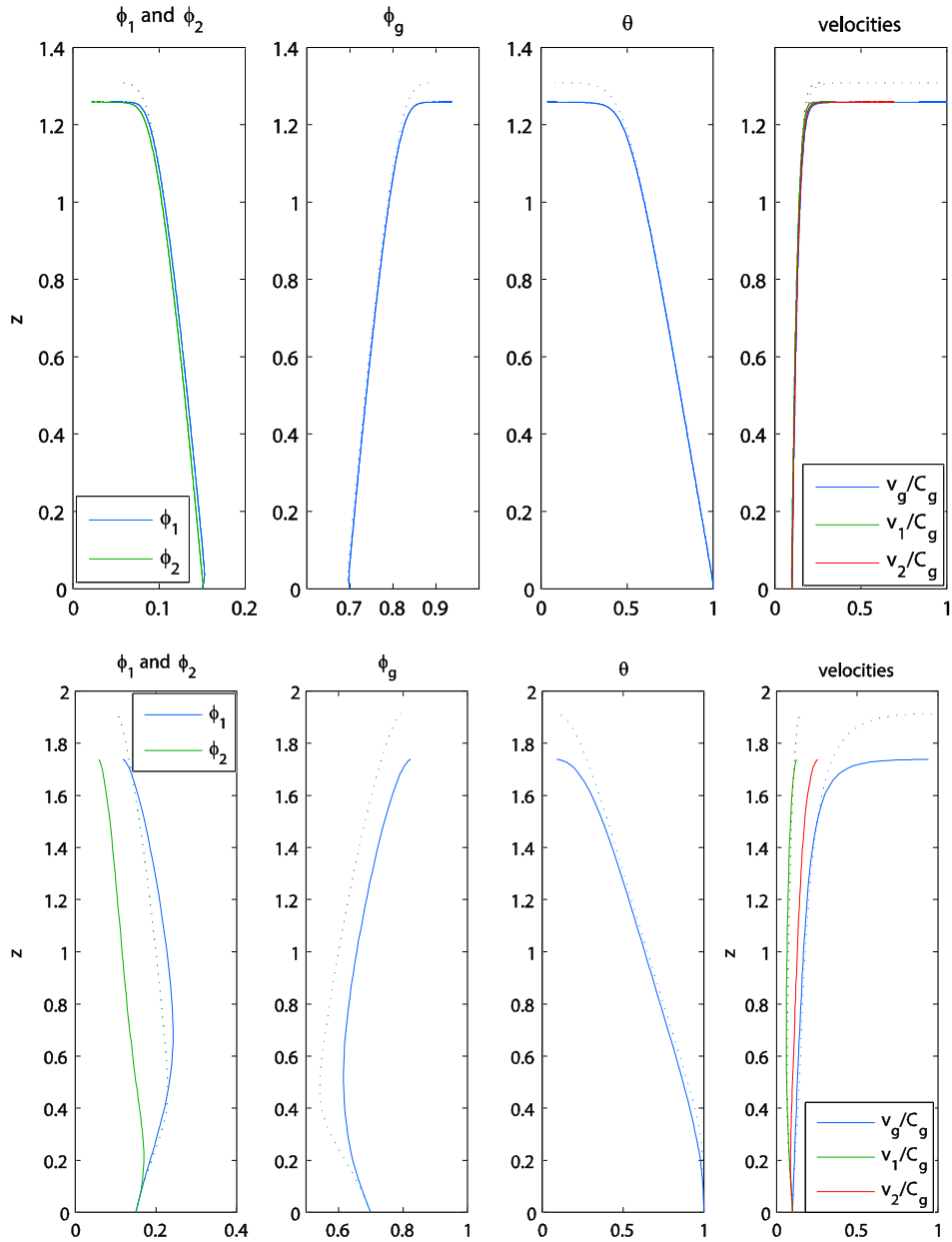

Figure 11. Solution to full equations for two-phase (dotted lines) and three-phase (solid lines) systems. In a two-phase system, (top row) $D_1^\tau = 75000$ and (bottom row) $D_1^\tau = 100$. In all cases, $D_1^0 = 1$. In a three-phase system, drag coefficients for the second solid phase were increased so that $D_1^0/D_2^0 = 0.01$ and $D_1^\tau/D_2^\tau = 0.1$ (second particle size was reduced 10 times). Note that the height of the choking front was reduced accordingly. In this example of a three-phase system, choking occurs at smaller values of θ and higher values of φ_g (higher degree of gas decompression and expansion).

(equation (37)). The exit velocity of the gas also depends on the decompression of gas density θ, which in itself depends on the density ratio β, parameter $\overline{\alpha}$, drag forces, and details of the size distribution (see equation (45)). Stronger gas decompression leads to higher exit velocities. The separation of solid and gas leads to choking velocities that approach the pure gas sound speed. In cases when the gas volume fraction does not have time to change significantly during the eruption, the gas exit velocity might even slightly exceed the pure gas sound speed. In either case, the gas velocity is significantly higher than the pseudogas choking velocity. The exit velocity of solid particles also can be very high (Figure 9) and depends strongly on the dimensionless parameter $\overline{\alpha}$, which reflects the fragmentation velocity and the gas volume fraction at which choking occurs. At high values of φ_g, the solid particle velocity might even approach the gas velocity.

©2015. The Authors.

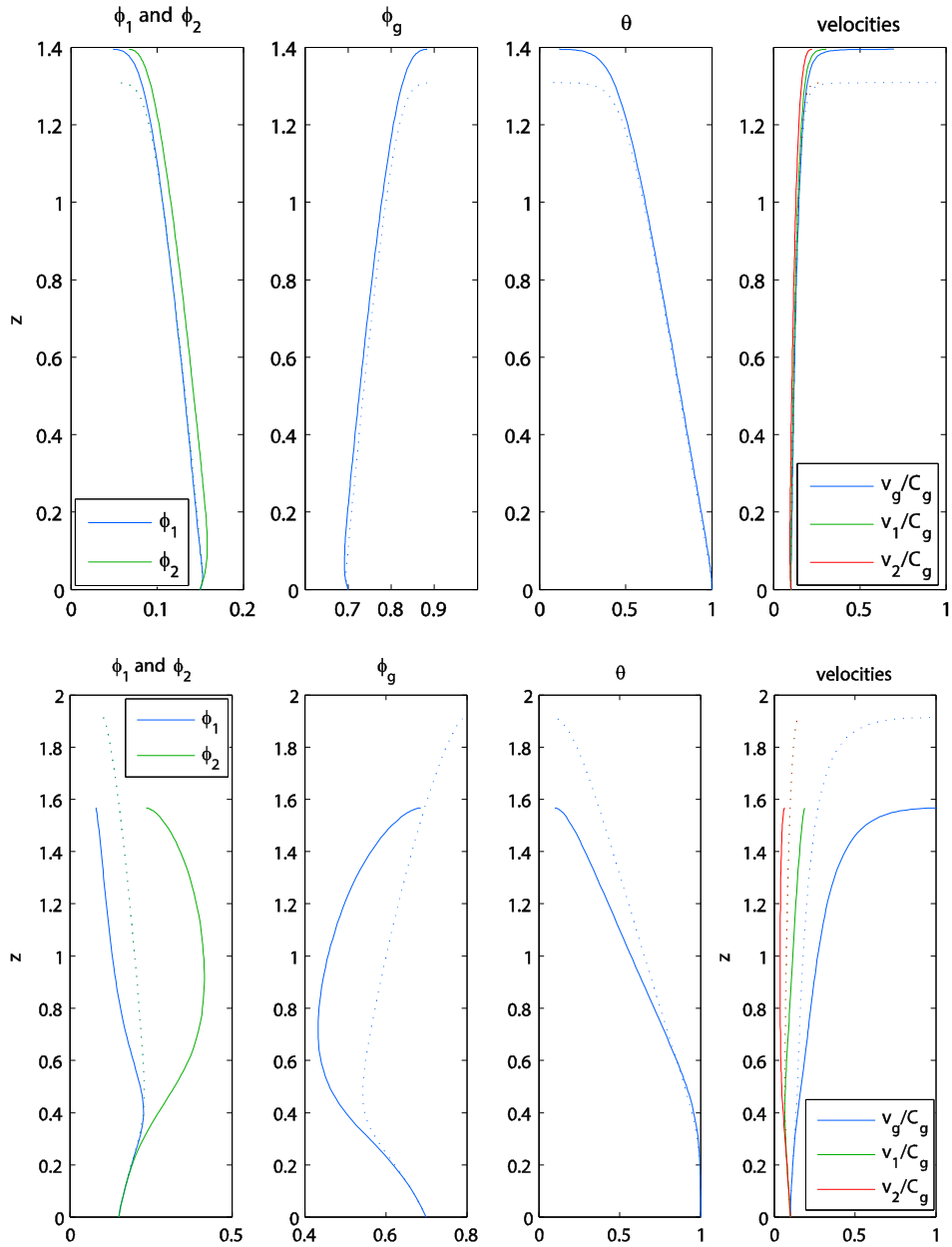

Figure 12. Solution to full equations for two-phase (dotted lines) and three-phase (solid lines) systems. In a two-phase system, (top row) $D_1^\tau = 75000$ and (bottom row) $D_1^\tau = 100$. In all cases, $D_1^0 = 1$. In a three-phase system, drag coefficients for the second solid phase were reduced so that $D_1^0/D_2^0 = 100$ and $D_1^\tau/D_2^\tau = 10$ (second particle size was increased ten times). Note that the height of the choking front is increased accordingly. In a three-phase system choking occurs at smaller values of φ_g.

However, since solid particles cannot move faster than the gas propelling them, the point at which $v_g = v_m$ marks the maximum possible φ_g at the choking point. For the case when $\varphi_{g0} = 0.7$ represented in Figure 9, $\varphi_{g,\max} = 0.97$ for $\overline{\alpha} = 10$ and $\varphi_{g,\max} = 0.99$ for $\overline{\alpha} = 50$. Whether this maximum value will be reached depends on the details of the full solution to equations (38) and (39) and the values of the drag coefficients D_1^0 and D_1^τ $(D_1^0 \ll D_1^\tau)$. The drag coefficients also determine the height z of the choking front in a conduit. Higher values of drag coefficients lead to higher choking values of φ_g and accordingly to higher values of v_m. Figure 10 shows an example of the full solution of the nonlinear steady state equations for two-phase system obtained numerically with an explicit Runge-Kutta method using a standard MATLAB solver. At $D_1^0 = 1$ and $D_1^\tau = 10^5$ exit velocities of solid particles are just 3.6 times less than the exit velocity of the gas. However,

©2015. The Authors.

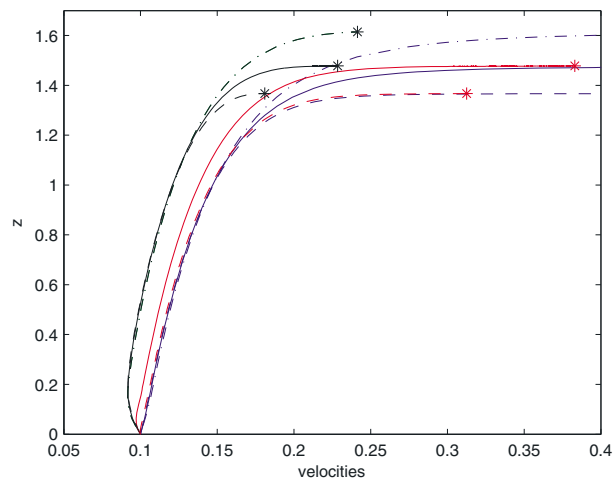

Figure 13. Solution to full equations for two different cases of three-phase systems. Velocities in a two-phase mixture are shown as dash-dotted lines for comparison. In three-phase systems one population has particles with the same size $r_1 = 10^{-2}$ as those in the basic two-phase mixture, while the second population is 10 times smaller (solid lines) or 200 times smaller (dashed lines). Drag coefficients are $D_1^0 = 0.2$ and $D_1^\tau = 3000$. Blue lines correspond to gas velocity, red lines show the velocity of smaller particles, and black lines mark the velocity of bigger particles. Choking velocities are indicated with stars. Notice that twentyfold reduction in the size of smaller particles leads to a lower choking point and lower exit velocities of both populations of particles (compare dashed and solid lines).

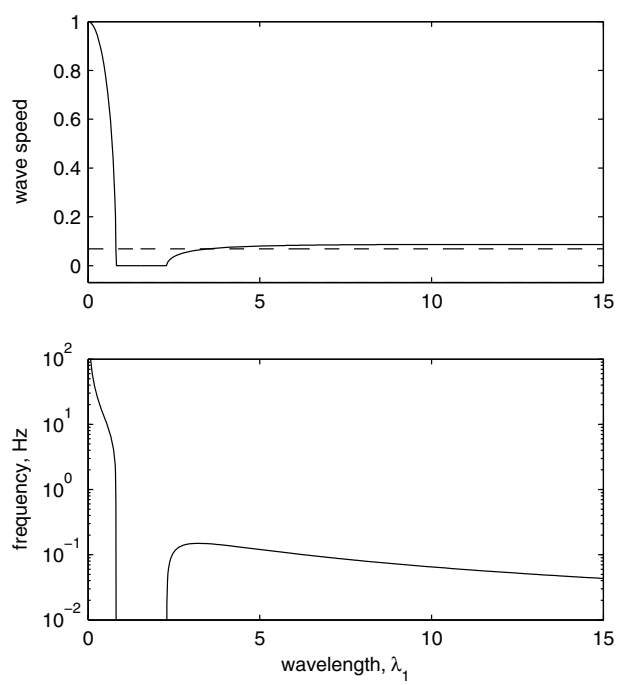

Figure 14. Nondimensional (top) wave speed and (bottom) frequency (hertz) as functions of nondimensional wavelength for the three-phase distribution with $\lambda_2/\lambda_1 = 15$ shown in Figure 4a. The frequencies of fast (0.63–500 Hz) and slow (0.04–0.15 Hz) waves are distinguished by the attenuation or mute gap separating lower-wavelength and higher-wavelength waves.

numerical solutions show that there is a limit that v_m can reach. Five orders of magnitude increase in D_1^τ still gives only $v_g/v_m = 2.5$.

In a three-phase mixture with solid particles of two different sizes, the exit velocities of solid particles are determined by their own volume fractions at the beginning of separation and at the choking point (see equations in (37)). The presence of an additional solid phase leads to the dependence of the choking velocity, in the gas and solid phases, on the actual distribution of particles and on their drag forces (Figures 11 and 12). In Figures 11 and 12 we consider cases where one population has particles with the same size as those in the basic two-phase mixture, while the second population is 10 times smaller (Figure 11) or 10 times bigger (Figure 12). In both cases, smaller particles travel faster than big particles. However, the presence of the second population of particles influences the choking velocity of the first population. In particular, the first population's choking velocity is faster than it would be in the simple two-phase system if the second population's particles are bigger, but slower otherwise. This happens due to the changes in the gas pressure induced by the relative motion of particles of different sizes. If the secondary particles are smaller they make the primary particles "feel" like they are moving through a dusty gas with slower sound speed, while if the secondary particles are big then the gas moves around them—as if they are nozzles and constrictions—which makes both the gas and primary particles faster. Furthermore, for a fixed primary population particle size, the decrease in size of smaller particles in the secondary population leads to lower exit velocities of both small and big particles (Figure 13). Thus, the exit velocities of the solid particles bear

©2015. The Authors.

information on their sizes and on their size distribution. The presence of the second particle phase affects gas density and gas volume fraction. Smaller secondary particles lead to choking at higher gas volume fractions and lower gas density, while larger secondary particles lead to eruptions at smaller gas volume fractions and higher gas density (Figures 11 and 12). At low values of D_1^τ and D_2^τ, the presence of the second population leads to lower choking point than in a reference two-phase mixture (Figures 11 and 12). However, at high values of D_1^τ and D_2^τ choking in a three-phase mixture might occur higher up (see Figure 12, top row).

6. Discussion and Conclusions

Explosive volcanic eruptions are critically dependent on choking conditions in the volcanic edifice, which are in turn governed by the characteristics of acoustic waves of the ash-gas mixture in the conduit. In this paper, we investigate the effect of ash particle mixture ratios and size distributions on acoustic wave propagation, shock wave development, and choking conditions. Both acoustic data and eruption velocities of solid particles are strongly influenced by the details of solid particle distributions. We show that solid particles of different sizes do not qualitatively change the acoustic spectrum, but they do change the wavelength range of different wave types. Eruptions with very different particle sizes (high λ_2/λ_1 ratio) have very narrow bands of fast "hot-gas" sound waves as well as narrow purely attenuating mute bands. Therefore, eruptions with a large amount of small ashes accompanying large particles will tend to have small-wavelength pressure variations. For example, if $\lambda_2/\lambda_1 = 15$ (i.e., $r_1^2/r_2^2 = 15$) as in Figure 4a, then fast sound waves would have dimensionless wavelengths ranging from 0 to 0.8. If we assume that initial gas density in a very compressed state is 100 kg/m^3, gas viscosity is $\mu = 10^{-5}$ Pa s, pure gas sound speed is $C_g = 600$ m/s, and a mean particle size is $r_1 = 2 \cdot 10^{-4}$ m then the dimensional wavelength ranges from 0 to $\lambda = 0.5\pi r_1^2 C_g \rho_0/\mu = 377$ m. This corresponds to the frequency ranging from 0.63 to 500 Hz (Figure 14). Fast sound waves in such eruptions are also strongly attenuated independently of their wavelength. More uniform particle size distributions with small standard deviation can have slightly wider bands of fast waves and "muteness". Thus, the structure of the acoustic spectrum, or dispersion relation, characterizes the degree of particle size variation.

At large wavelength the speed of acoustic waves in a polydispersed mixture approaches that of the pseudogas, which validates the pseudogas approximation for long waves. The frequencies of fast and slow waves are also distinct. Fast waves have high frequencies spanning from 0.63 Hz up to more than 500 Hz (see Figure 14). Low frequencies (0.04–0.15 Hz in Figure 14) characterize slow waves, for which the peak frequency is shifted toward relatively small wavelength ($\lambda_1 = 3.2$ in Figure 14). Frequencies in between these two limits are blocked. Slow waves have much lower attenuation. Therefore, for a sustained vertical eruption the recorded acoustic signal will be dominated by the low frequency of the large pseudogas wavelengths, especially far from the eruption. Indeed, recent observations by *Fee et al.* [2010a] who recorded Strombolian to Plinian activity from Tungurahua Volcano in Ecuador show that most of the seismic energy release corresponds to relatively narrow band of low frequencies with the dominant frequency ranging from 0.25 Hz to below 0.1 Hz for a sustained plinian eruption. For each eruption, the dominant frequency depends mostly on the particle size and also on the properties of the surrounding gas (ρ_0, β, μ, and φ_{g0}) and a number of different particle populations. One order of magnitude decrease in the dominant (coarse) particle size leads to almost 2 orders of magnitude increase in the peak frequency. The presence of the secondary population of fine particles further increases the peak frequency. Thus, our model predicts that the presence of fine ash broadens the emitted frequency range, which is consistent with observations by *Fee et al.* [2010a]. Furthermore, our model shows that the signal recorded in *Fee et al.* [2010a] of less than 0.5 Hz is consistent with a dominant particle size of 350 μm (as given by *Eychenne et al.* [2012]) and characteristic values for the other parameters. Thus, systematic acoustic measurements/records of eruption at Tungurhua and other explosive volcanoes associated with this analysis could give information on the dominant particle size of the plume and help assess risk at a given volcano.

Eruption velocities, choking, and the structure of the erupting column in the conduit are revealed by steady state nonlinear 1-D analysis of the two-phase polydisperse system. The degree of gas depressurization at choking depends mostly on the initial velocity at the fragmentation point relative to the pure gas sound speed ($\overline{\alpha}$). A fast ascending ash-gas mixture has higher gas density (θ) on exiting the conduit because the mixture does not have sufficient time to depressurize. As expected, both faster initial velocities (lower $\overline{\alpha}$) and lower particle-to-gas density ratio (β) lead to faster exit velocities and hence potentially higher eruption

©2015. The Authors.

columns. However, the size distribution of particles also strongly affects the exit velocity distribution of the solid particles as well as the gas content and density at the choking point. Indeed, smaller particles not only travel faster than the bigger ones but they influence the velocity of bigger particles and vice versa. That is, given a fixed primary particle population, secondary particles will speed up or slow down the primary particles if they are larger or smaller than the primary particles, respectively. Furthermore, a large difference between primary and secondary particles leads to choking at higher gas volume fractions and lower gas density, while distributions with primary and secondary particles of comparable sizes lead to eruptions at smaller gas volume fractions and higher gas density. Consequently, the size distribution of particles, in general, and the presence of different populations of particles of different sizes should influence the dynamics of the explosion at the vent.

In particular, our model suggests that a bimodal distribution in particle size should favor the development of lateral flows at the vent, while unimodal particle distributions favor a vertical eruption. Indeed, if we consider a bimodal distribution with large primary and small secondary particles and compare it to a unimodal distribution with particles of the same size as large particles in the bimodal case (as in Figures 11 and 12) then the presence of smaller particles tends to decelerate the bigger particles. The velocity of the primary population depends not only on the presence of the secondary particles but also on their size (Figure 13). The smaller the sizes in the secondary population, the slower the primary particles become. Therefore, in eruptions with large amount of very fine ash, the bigger particles would be effectively slowed down and more likely decelerate and be deviated from a vertical trajectory into a lateral copyroclastic flow. In such a way, very fast moving particles in unimodal mixtures would be lofted higher and spread less laterally. This is consistent with observations [*Evans et al*., 2009] and suggests that two-phase dynamics can be responsible for the variations in the eruption style. However, our model only constrains the initial conditions for collapsing gravity currents (i.e., it sets the initial state of the collapsing column or spike), which describe the zeroth order behavior of most volcanic lateral flows [*Huppert*, 2006].

Overall, the mixture of small and course particles leads to an effective three-phase mixture that could result in the development of lateral copyroclastic flows with a buoyant cloud made of very fine ash that can be propelled very high into the atmosphere. This interaction between different particle sizes (via momentum transfer through the gas phase) would explain the common observation of simultaneous buoyant vertical plumes and pyroclastic density currents at silicic volcanoes [*Cashman and Sparks*, 2013; *Clarke et al*., 2002]. Deposits from plinian explosive silicic explosion indeed contain a large content of fine and very fine ash (up to 50% [*Rose and Durant*, 2009]). For instance, 70% of the total mass of the well-known Waimihia and Hatepe plinian deposits from the rhyolitic Taupo volcanic center is made of particles finer than 500 μm [*Walker*, 1981]. These silicic plinian eruptions are also associated with abundant copyroclastic flows. For instance, the plinian eruption of Mount St. Helens in May 1980 was accompanied by abundant copyroclastic flows and the total grain size distribution of the deposits shows a distribution characterized by two peaks, one around $\phi = 2$ to 3 (diameter $d = 125$–$250\ \mu$m) and the largest around $\phi = 6$ ($d = 15\ \mu$m) [*Carey and Sigurdsson*, 1982; *Rose and Durant*, 2009]. Similarly, *Dartevelle et al*. [2002] proposed that the Mount Pinatubo 1991 eruption's volcanic ash deposits were substantially derived from coignimbrite clouds, and not only by a Plinian cloud, because the deposits are substantially rich in very fine ashes (they contain 5–25% of ashes $< 10\ \mu$m).

In contrast, more mafic explosive eruptions tend to show a much smaller content in fine ash (only a few percent [*Rose and Durant*, 2009]) even when they develop a sustained vertical column for hours. Copyroclastic flows are not always present or only minor to subplinian events. When available, total grain size distributions for more mafic explosive eruptions indeed show that vertical eruptions are generally unimodal, while lateral eruptions are often bimodal. For instance the total grain size distribution of the subplinian deposits of the Ruapehu Volcano, New Zealand, erupted on June 1996, shows a Gaussian distribution (independently of the technique used) centered at $\phi = -1$ to 2 (i.e., mean diameter between 2 and 0.25 mm) depending on the technique [*Bonadonna and Houghton*, 2005]. The Ruapehu eruption did not show pyroclastic flows. The 1974 Fuego eruption, Guatemala, produced a sustained column for 5 h but had a very low proportion of fine particles [*Rose and Durant*, 2009]. The total grain size distribution of the 14 October subplinian ejecta also yields a relatively coarse and unimodal initial population with a median value of ϕ equal to 0.58 corresponding to a diameter between 0.5 and 1 mm [*Rose et al*., 2008]. This eruption produced minor copyroclastic flows that are, on the contrary, characterized by a large amount of fine ashes [*Rose et al*., 2008]. The Chaimilla deposit was produced by mafic explosive eruptions at Villarrica Volcano, Southern Andes, in the late Holocene [*Costantini et al*., 2011].

©2015. The Authors.

The fallout units are characterized by a unimodal size distribution with a median value of ϕ between -1 and -3 (i.e., median diameter between 2 and 8 mm). On the contrary, the pyroclastic density current deposit (unit E) shows a bimodal grain size distribution with a significant amount of fine ash, but the median diameter is similar to the other fallout samples [*Costantini et al.*, 2011]. Similarly, analysis of andesitic eruption deposits occurring during 2004–2006 at Volcan de Colima, Mexico, shows a marked difference between samples from separate vertical eruptions and copyroclastic flows. The particle size distribution of vertical eruptions is more peaked (at $\phi = 4$) than copyroclastic samples, which shows a bimodal size distribution with a high proportion of very fine ash ($<30\,\mu$m) [*Evans et al.*, 2009].

Furthermore, the difference in fine ash content between silicic and more mafic explosions might be linked to the process of bubble nucleation and growth and gas escape in two different types of liquid marked by very different viscosities [*Rose and Durant*, 2009; *Rust and Cashman*, 2011]. In mafic melts the diffusion of volatiles, flow, growth, and expansion of bubbles are facilitated because viscosity is smaller and temperature is higher than for more silicic magmas. This could yield a unimodal size distribution for bubbles, with bias toward big bubbles, and a single fragmentation event leading to unimodal size distribution biased toward larger particle sizes, thereby causing a vertical subplinian eruption. In more viscous silicic melt, diffusion of volatiles is more difficult, the flow of bubbles in the melt is slow, coalescence might be more difficult, but there are more volatiles (hence probably many small bubbles nucleating), and this could lead to a wider bubble size distribution. Following the idea of *Kaminski and Jaupart* [1998], fragmentation in silicic melt might thus happen in several steps. If there is only one fragmentation step because the eruption is not very powerful, only the bigger bubbles and part of the smaller ones fragment (many of the smaller ones get trapped in the pumice), and this would lead to polymodal particle size distribution that favors lateral eruptions. If the eruption is very powerful, there would be a complete fragmentation, which would lead to one, very fine, particle size and a (high) plinian eruption. This would explain that (1) more mafic explosions tend to develop vertical eruptions (because of their unimodal distributions) and not much lateral eruptions, while more silicic explosions tend to develop more lateral eruptions, and (2) more mafic eruptions show unimodal size particle distribution with a mean grain in general larger than more silicic eruptions. Taken altogether, our modeling and these observations would suggest that the presence of large amounts of fine ashes in copyroclastic silicic fall might be inherent to the initial fragmentation sequence [*Kaminski and Jaupart*, 1998; *Rust and Cashman*, 2011], whereas subsequent evolution of particle sizes in volcanic conduits [*Dufek et al.*, 2012] and/or comminution and milling in pyroclastic flows might be less important in producing fine ashes.

Finally, the vertical size distribution of particles within the eruption column and the horizontal distribution of sizes in the resulting pyroclastic deposits around the crater can be used to extract information on the initial and final volume fractions of solid particles as well as on the degree of gas expansion. For example, if the choking velocities of the gas v_g and the two populations of particles v_1 and v_2 are measured, and the proportions of small and big particles in a volcanic pumice ($\varphi_2/\varphi_1 = \kappa$) are inferred from pyroclastic deposits, then three equations (37) together with choking condition (46) (along with the constraints that $\varphi_1 + \varphi_2 + \varphi_g = \varphi_{10} + \varphi_{20} + \varphi_{g0} = 1$) allow the determination of all volume fractions and the relative gas density θ as functions of fragmentation velocity W_0. Thus, in the end, the physics of two-phase polydisperse eruptions can further elucidate the connection between eruption products and the internal dynamics of the volcanic conduit.

Acknowledgments
This work is purely theoretical and makes no use of any specific data other than standard mathematical models described above. All the results of the paper can be reproduced following derivations specified in the text of the paper. This work was supported in part by a grant (EAR-1015229) from the National Science Foundation (for D.B.), IFE's strategic funds (for V.Y.), and ALEAS/INSU (for C.M.).

References

Beetstra, R., M. A. van der Hoef, and J. A. M. Kuipers (2007), Drag force of intermediate Reynolds number flow past mono- and bidisperse arrays of spheres, *AiChe J.*, *53*(2), 489–501.

Bercovici, D., and C. Michaut (2010), Two-phase dynamics of volcanic eruptions: Compaction, compression and the conditions for choking, *Geophys. J. Int.*, *182*(2), 843–864.

Bercovici, D., A. M. Jellinek, C. Michaut, D. C. Roman, and R. Morse (2013), Volcanic tremors and magma wagging: Gas flux interactions and forcing mechanism, *Geophys. J. Int.*, *195*(2), 1001–1022.

Bonadonna, C., and B. F. Houghton (2005), Total grain-size distribution and volume of tephra-fall deposits, *Bull. Volcanol.*, *67*(5), 441–456.

Bourbié, T. (1987), *Acoustics of Porous Media*, vol. 16, p. 334, Editions Technip, Paris.

Carey, S. N., and H. Sigurdsson (1982), Influence of particle aggregation on deposition of Distal Tephra from the May 18, 1980, eruption of Mount St-Helens volcano, *J. Geophys. Res.*, *87*(Nb8), 7061–7072, doi:10.1029/JB087iB08p07061.

Cashman, K. V., and R. S. J. Sparks (2013), How volcanoes work: A 25 year perspective, *Geol. Soc. Am. Bull.*, *125*(5–6), 664–690.

Chojnicki, K., A. B. Clarke, and J. C. Phillips (2006), A shock-tube investigation of the dynamics of gas-particle mixtures: Implications for explosive volcanic eruptions, *Geophys. Res. Lett.*, *33*, L15309, doi:10.1029/2006GL026414.

Chouet, B. (2003), Volcano seismology, *Pure Appl. Geophys.*, *160*(3–4), 739–788.

 ©2015. The Authors.

Clarke, A. B., B. Voight, A. Neri, and G. Macedonio (2002), Transient dynamics of vulcanian explosions and column collapse, *Nature*, *415*(6874), 897–901.
Costantini, L., L. Pioli, C. Bonadonna, J. Clavero, and C. Longchamp (2011), A Late Holocene explosive mafic eruption of Villarrica volcano, Southern Andes: The Chaimilla deposit, *J. Volcanol. Geotherm. Res.*, *200*(3–4), 143–158.
Crowe, C. T., M. Sommerfeld, and Y. Tsuji (1998), *Multiphase Flows With Droplets and Particles*, p. 471, CRC Press, Boca Raton, Fla.
Dartevelle, S., G. G. J. Ernst, J. Stix, and A. Bernard (2002), Origin of the Mount Pinatubo climactic eruption cloud: Implications for volcanic hazards and atmospheric impacts, *Geology*, *30*(7), 663–666.
Drew, D. A., and S. L. Passman (1999), *Theory of Multicomponent Fluids*, p. 308, Springer, New York.
Dufek, J., M. Manga, and A. Patel (2012), Granular disruption during explosive volcanic eruptions, *Nat. Geosci.*, *5*(8), 561–564.
Edelman, I. (2004), Surface waves at vacuum/porous medium interface: Low frequency range, *Wave Motion*, *39*(2), 111–127.
Evans, J. R., J. E. Huntoon, W. I. Rose, N. R. Varley, and J. A. Stevenson (2009), Particle sizes of andesitic ash fallout from vertical eruptions and co-pyroclastic flow clouds, Volcan de Colima, Mexico, *Geology*, *37*(10), 935–938.
Eychenne, J., J. L. Le Pennec, L. Troncoso, M. Gouhier, and J. M. Nedelec (2012), Causes and consequences of bimodal grain-size distribution of tephra fall deposited during the August 2006 Tungurahua eruption (Ecuador), *Bull. Volcanol.*, *74*(1), 187–205.
Fee, D., M. Garces, and A. Steffke (2010a), Infrasound from Tungurahua volcano 2006–2008: Strombolian to Plinian eruptive activity, *J. Volcanol. Geotherm. Res.*, *193*(1–2), 67–81.
Fee, D., M. Garces, M. Patrick, B. Chouet, P. Dawson, and D. Swanson (2010b), Infrasonic harmonic tremor and degassing bursts from Halema'uma'u Crater, Kilauea Volcano, Hawaii, *J. Geophys. Res.*, *115*, B11316, doi:10.1029/2010JB007642.
Gubaidullin, D. A., and R. I. Nigmatulin (2000), On the theory of acoustic waves in polydispersed gas-vapor-droplet suspensions, *Int. J. Multiphase Flow*, *26*(2), 207–228.
Gubaidullin, D. A., A. A. Nikiforov, and E. A. Utkina (2011), Acoustic waves in two-fraction mixtures of gas with vapor, droplets and solid particles of different materials and sizes in the presence of phase transitions, *Fluid Dyn.*, *46*(1), 72–79.
Hill, R. J., D. L. Koch, and A. J. C. Ladd (2001), Moderate-Reynolds-number flows in ordered and random arrays of spheres, *J. Fluid Mech.*, *448*, 243–278.
Holloway, W., X. L. Yin, and S. Sundaresan (2010), Fluid-particle drag in inertial polydisperse gas-solid suspensions, *AiChe J.*, *56*(8), 1995–2004.
Huppert, H. E. (2006), Gravity currents: A personal perspective, *J. Fluid Mech.*, *554*, 299–322.
Ishii, R., and H. Matsuhisa (1983), Steady reflection, absorption and transmission of small disturbances by a screen of dusty gas, *J. Fluid Mech.*, *130*(May), 259–277.
Jaupart, C., and S. Tait (1990), Dynamics of eruptive phenomena, *Rev. Mineral Geochem.*, *24*, 213–238.
Jellinek, A. M., and D. Bercovici (2011), Seismic tremors and magma wagging during explosive volcanism, *Nature*, *470*(7335), 522–525, U109.
John, J. E. A. (1969), *Gas Dynamics*, 394 pp., Allyn and Bacon, Boston.
Johnson, J. B., R. C. Aster, and P. R. Kyle (2004), Volcanic eruptions observed with infrasound, *Geophys. Res. Lett.*, *31*, L14604, doi:10.1029/2004GL020020.
Kaminski, E., and C. Jaupart (1998), The size distribution of pyroclasts and the fragmentation sequence in explosive volcanic eruptions, *J. Geophys. Res.*, *103*(B12), 29,759–29,779, doi:10.1029/98JB02795.
Kieffer, S. W. (1977), Sound speed in liquid-gas mixtures—Water-air and water-steam, *J. Geophys. Res.*, *82*(20), 2895–2904, doi:10.1029/JB082i020p02895.
Kozono, T., and T. Koyaguchi (2009a), Effects of relative motion between gas and liquid on 1-dimensional steady flow in silicic volcanic conduits: 1. An analytical method, *J. Volcanol. Geotherm. Res.*, *180*(1), 21–36.
Kozono, T., and T. Koyaguchi (2009b), Effects of relative motion between gas and liquid on 1-dimensional steady flow in silicic volcanic conduits: 2. Origin of diversity of eruption styles, *J. Volcanol. Geotherm. Res.*, *180*(1), 37–49.
Lopatnikov, S. L., and A. H. D. Cheng (2004), Macroscopic Lagrangian formulation of poroelasticity with porosity dynamics, *J. Mech. Phys. Solids*, *52*(12), 2801–2839.
Manga, M., A. Patel, and J. Dufek (2011), Rounding of pumice clasts during transport: Field measurements and laboratory studies, *Bull. Volcanol.*, *73*(3), 321–333.
Mitchell, K. L. (2005), Coupled conduit flow and shape in explosive volcanic eruptions, *J. Volcanol. Geotherm. Res.*, *143*(1–3), 187–203.
Neri, A., T. E. Ongaro, G. Macedonio, and D. Gidaspow (2003), Multiparticle simulation of collapsing volcanic columns and pyroclastic flow, *J. Geophys. Res.*, *108*(B4), 2202, doi:10.1029/2001JB000508.
Nigmatulin, R. I. (1991), *Dynamics of Multiphase Media*, 878 pp., Hemisphere Pub. Corp, New York.
Rose, W. I., and A. J. Durant (2009), Fine ash content of explosive eruptions, *J. Volcanol. Geotherm. Res.*, *186*(1–2), 32–39.
Rose, W. I., S. Self, P. J. Murrow, C. Bonadonna, A. J. Durant, and G. G. J. Ernst (2008), Nature and significance of small volume fall deposits at composite volcanoes: Insights from the October 14, 1974 Fuego eruption, Guatemala, *Bull. Volcanol.*, *70*(9), 1043–1067.
Rust, A. C., and K. V. Cashman (2011), Permeability controls on expansion and size distributions of pyroclasts, *J. Geophys. Res.*, *116*, B11202, doi:10.1029/2011JB008494.
Vergniolle, S., and C. Jaupart (1986), Separated 2-phase flow and basaltic eruptions, *J. Geophys. Res.*, *91*(B12), 12,842–12,860, doi:10.1029/JB091iB12p12842.
Vergniolle, S., G. Brandeis, and J. C. Mareschal (1996), Strombolian explosions: 2. Eruption dynamics determined from acoustic measurements, *J. Geophys. Res.*, *101*(B9), 20,449–20,466, doi:10.1029/96JB01925.
Walker, G. P. L. (1980), The Taupo Pumice—Product of the most powerful known (ultraplinian) eruption, *J. Volcanol. Geotherm. Res.*, *8*(1), 69–94.
Walker, G. P. L. (1981), The Waimihia and Hatepe Plinian deposits from the Rhyolitic Taupo volcanic center, *N. Z. J. Geol. Geophys.*, *24*(3), 305–324.
Wilson, L. (1976), Explosive volcanic eruptions: 3. Plinian eruption columns, *Geophys. J. R. Astron. Soc.*, *45*(3), 543–556.
Wilson, L., R. S. J. Sparks, and G. P. L. Walker (1980), Explosive volcanic-eruptions: 4. The control of magma properties and conduit geometry on eruption column behavior, *Geophys. J. R. Astron. Soc.*, *63*(1), 117–148.
Woods, A. W. (1995), The dynamics of explosive volcanic-eruptions, *Rev. Geophys.*, *33*(4), 495–530, doi:10.1029/95RG02096.
Yin, X. L., and S. Sundaresan (2009), Fluid-particle drag in low-Reynolds-number polydisperse gas-solid suspensions, *AiChe J.*, *55*(6), 1352–1368.

 ©2015. The Authors.